

# Optical Control of Multistage Phase Transition via Phonon Coupling in MoTe<sub>2</sub>

Meng-Xue Guan<sup>1,2,\*</sup>, Xin-Bao Liu<sup>1,2,\*</sup>, Da-Qiang Chen<sup>1,2</sup>, Xuan-Yi Li<sup>1,2</sup>, Ying-Peng Qi<sup>3</sup>,  
Qing Yang<sup>1,2</sup>, Pei-Wei You<sup>1,2</sup>, and Sheng Meng<sup>1,2,4,†</sup>

<sup>1</sup>*Beijing National Laboratory for Condensed Matter Physics and Institute of Physics,  
Chinese Academy of Sciences, Beijing 100190, China*

<sup>2</sup>*School of Physical Sciences, University of Chinese Academy of Sciences, Beijing 100190, China*

<sup>3</sup>*Center for Ultrafast Science and Technology, School of Physics and Astronomy,  
Shanghai Jiao Tong University, Shanghai 200240, China*

<sup>4</sup>*Songshan Lake Materials Laboratory, Dongguan, Guangdong 523808, China*

(Received 5 August 2021; revised 28 November 2021; accepted 7 December 2021; published 3 January 2022)

The temporal characters of laser-driven phase transition from  $2H$  to  $1T'$  has been investigated in the prototype MoTe<sub>2</sub> monolayer. This process is found to be induced by fundamental electron-phonon interactions, with an unexpected phonon excitation and coupling pathway closely related to the nonequilibrium relaxation of photoexcited electrons. The order-to-order phase transformation is dissected into three substages, involving energy and momentum scattering processes from optical ( $A'_1$  and  $E'$ ) to acoustic phonon modes [LA(M)] in subpicosecond timescale. An intermediate metallic state along the nonadiabatic transition pathway is also identified. These results have profound implications on non-equilibrium phase engineering strategies.

DOI: 10.1103/PhysRevLett.128.015702

Controlling the phase of matter via coherent excitation of electron and phonon subsystems has long been an attractive goal for ultrafast science [1–12]. During phase transitions, the energy dissipation will lead to complicated relaxation pathways for both fermionic (e.g., electrons) and bosonic quasiparticles (e.g., phonons, magnons), which might involve scatterings among different phonon modes [13–16]. Understanding the complex interactions requires theoretical modeling that is capable of disentangling the interplay among different degrees of freedom, which also provides powerful tools to decode vast information underneath the experimentally detected spectroscopic signals.

Monolayer (1L) MoTe<sub>2</sub> is a prototypical example for photoinduced phase transitions. Its stable semiconducting  $2H$  and metastable metallic  $1T'$  phases have quite a small energy difference [ $\sim 0.042$  eV per formula unit (f.u.)] among all transition-metal dichalcogenides (TMDs). The low-energy cost of such a transition has triggered great interest for broad device applications [17,18], and significant efforts have been made to achieve this goal through thermal annealing [19], strain [20], carrier doping [21], and laser irradiation [22].

The experimental identification of the phase transition was usually based on the evolution of Raman spectra [21,22], whereas the signals are insufficient to reveal the complete microscopic dynamics, due to the fact that only zone-center optical phonons are detected and ultrafast time-resolved information is usually lacking. Although greatly contributing to the understanding of the thermodynamic aspect of phase transition, theoretical analyses based on the

ground-state total-energy calculations have severe limitations in describing nonequilibrium processes, where the phase transition pathway is rather speculative and still under debate [23,24].

Here we aim at disentangling the coherent electron and lattice dynamics during laser driven  $2H$  to  $1T'$  phase transition of 1L-MoTe<sub>2</sub> based on real-time time-dependent density functional theory molecular dynamics (TDDFT-MD) simulations [25]. We found that structural distortions can be dissected into three substages, involving energy and momentum scattering processes from optical to acoustic phonon modes in  $q$  space. The initial population and decay of the optical  $A'_1$  and  $E'$  phonon modes originate from carrier excitation and cooling via strong electron-phonon couplings, and therefore, are closely related to laser parameters. The anharmonic motion of these two modes and the ultrafast ( $\sim 0.4$  ps) couplings to the longitudinal acoustic mode at the  $M$  point [LA( $M$ )] lead to a metallic intermediate state ( $2H^*$ ), which greatly reduces the activation energy barrier to form  $1T'$  phase. The ordered structural distortion is distinct from thermally driven phase transitions by selective excitation and the successive scattering of specific phonon modes.

The  $2H$  and  $1T'$  phase of 1L-MoTe<sub>2</sub> have an  $ABA$  and  $ABC$  stacking of the Te–Mo–Te sandwich structure, where the Mo site is in a hexagonal and distorted octahedral coordinate, respectively [51] [Figs. 1(a)–1(c)]. Along the adiabatic phase transition pathway, the kinetic barrier ( $E_b = 0.77$  eV/f.u.) is much larger than thermal fluctuations [Fig. 1(d)], and requires a high temperature ( $>500$  °C)

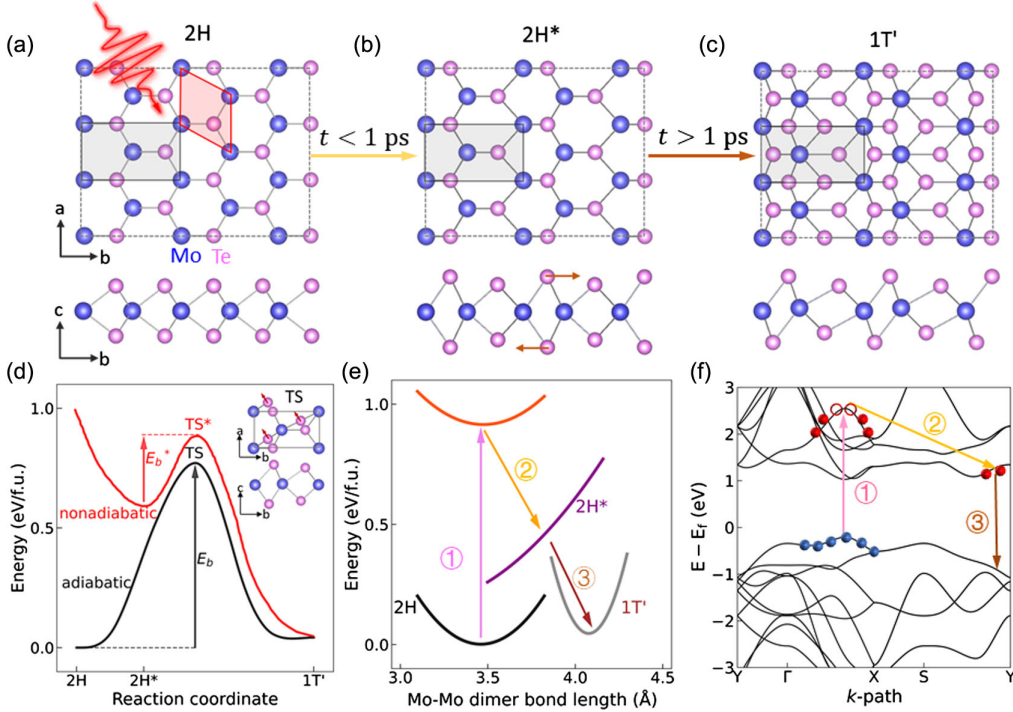


FIG. 1. (a)–(c) Atomic structures of initial ( $2H$ ), intermediate ( $2H^*$ ), and final ( $1T'$ ) states. The gray and red shadows in (a) represent the rectangular computational cell and the primitive cell of the  $2H$  phase. The arrows in (b) label the interlayer displacement of two Te layers after the participation of the  $E''$  mode from  $0.7$  ps. (d) Energy profile of  $1L\text{-MoTe}_2$  along the phase transition pathway from the  $2H$  to  $1T'$  phases. The inset shows the atomic structure of transition state ( $TS$ ) along the adiabatic transition path, and the arrows are used to represent the relative displacement of interlayer Te atoms. (e) Potential energy surfaces (PESs) of  $1L\text{-MoTe}_2$  before and after photoexcitation. The arrows are used to label the three substages of phase transition. (f) Schematic of carrier excitation (arrow ①) and relaxation (arrows ② and ③) pathways in the  $2H$  state. The hot and band-edge electrons lead to the successive emission of phonon modes that induce the phase transition.

to trigger structural instability of the  $2H$  phase [19]. The activation energy barrier will be significantly reduced to  $E_b^*$  upon the optically induced carrier excitation [52–54], and the dynamically unstable  $2H$  phase will obtain enough energy to overcome the activation barrier, leading to a structural transition (Supplemental Material Fig. S1 [25]). During the phase transition, a distinct transition pathway induced by the nonadiabatic coupling (i.e., the correlated electron-phonon dynamics beyond the Born-Oppenheimer approximation) is expected [25].

The calculations were performed using the  $4 \times 3\sqrt{3}$  supercell of  $2H\text{-MoTe}_2$ . The minimum rectangular supercell will fold the  $M$  point in the reciprocal space of the hexagonal primitive cell to the  $\Gamma$  point [Fig. S2(a) [25]]. Krishnamoorthy *et al.* demonstrated that the phonon modes at the  $M$  point establish an obviously softening upon strong field excitation [53]. Therefore, in the chosen supercell, the phonon modes at the  $\Gamma$  point will play the dominant roles in triggering phase transitions [Figs. S2(b)–2(d) [25]].

Optical pumping of electrons can generate pronounced changes in the potential energy surface and lead to the excitation of certain vibrational modes connected to phase transitions [4,52,55,56]. To investigate the phase transition of  $1L\text{-MoTe}_2$  driven by laser excitation, two

laser pulses with different intensities are applied to its  $2H$  phase. Under the illumination of moderate (fluence  $J = 1.17$  mJ/cm $^2$  and peak amplitude  $E_0 = 0.1$  V/Å) and relatively intense ( $J = 2.07$  mJ/cm $^2$ ,  $E_0 = 0.13$  V/Å) laser pulses, there are 2.31% and 6.81% carriers excited to the conduction bands (Fig. S3 [25]). The structural distortion is characterized by three parameters evaluated during the MD simulations, i.e., Mo–Mo dimer bond length variation ( $\Delta l$ ), out-of-plane length difference between the two pairs of vertical stacking Te atoms ( $\Delta z = z_2 - z_1$ ), and the averaged in-plane atomic displacement of two Te layers ( $d_1$  and  $d_2$ ).

Figures 2(a)–2(b) show the results under the moderate laser field. It is obvious that both  $\Delta l$  and  $\Delta z$  are nearly zero, indicating that the relative position of Mo ions and the out-of-plane flatness keep unchanged. Meanwhile, the in-phase atomic movement of the two Te layers indicates that the structural distortion of the  $2H$  phase is oscillating harmonically around its equilibrium position. When laser intensity is large enough to excite plenty of carriers, the coupling strength between lattice and carriers will be enhanced during the energy relaxation, which might steer the system towards states far from equilibrium and induce the emergence of new phonon modes [57].

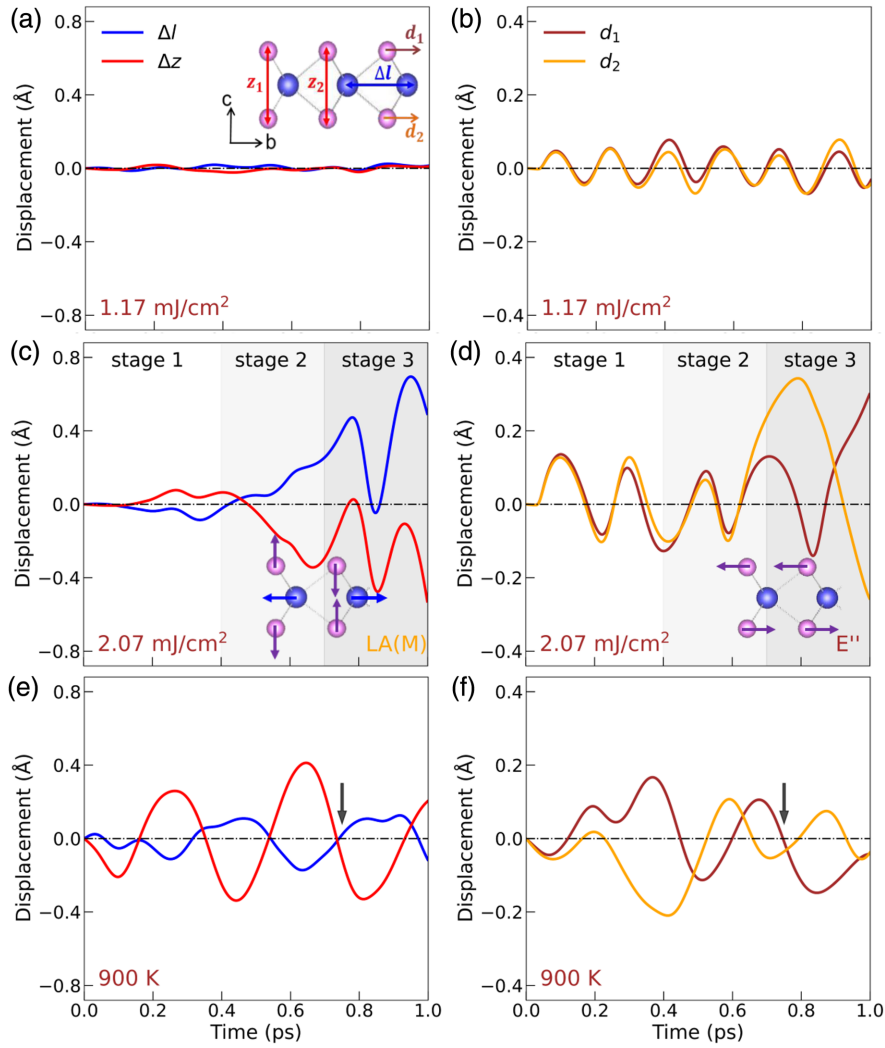


FIG. 2. (a)–(b) Time evolution of three structural parameters under the moderate laser field ( $1.17 \text{ mJ/cm}^2$ ), as defined in the inset. (c)–(d) and (e)–(f) are analogous to (a)–(b), but are the results under the strong laser field ( $2.07 \text{ mJ/cm}^2$ ) and thermal ( $900 \text{ K}$ ) excitation. Arrows in (e)–(f) are used to label the time from when the photoinduced and thermally driven structural distortions behave similarly.

Under the illumination of intense laser field, the structural evolution shows a distinct behavior, which can be divided into three stages [Fig. 2(c)–2(d)]. The first stage ( $0 \sim 0.4 \text{ ps}$ ) resembles the condition that is described above. Although the absolute values of  $\Delta l$  and  $\Delta z$  increase slowly after the end of laser pulse ( $t = 60 \text{ fs}$ ), the distortion is insufficient to destroy the geometry features of the  $2H$  phase. In the second stage ( $0.4 \sim 0.7 \text{ ps}$ ), accompanying with the rapid increase of Mo–Mo bond length, the out-of-plane wrinkling of Te atoms is also enhanced, following the geometry relationship and the Poisson ratio exhibited by the Mo–Te–Mo–Te parallelogram. It indicates that a new phonon mode starts to participate in the electron-phonon couplings. After  $0.7 \text{ ps}$ , different from the above two stages, the asynchronous interlayer displacements of Te atoms have been particularly evident and eventually the two layers move in opposite directions along the crystalline  $b$  axis. The characteristic behaviors at different timescales reveal

that the phonon scatterings are of significant importance in inducing the complex phase transition processes.

The relative contribution of different phonon modes along the phase transition pathway is distinguished via projecting atomic displacements onto vibrational eigenmodes at the  $\Gamma$  point of the rectangular supercell. At low excitation density, only two phonon modes are excited (Fig. S4 [25]), i.e., the out-of-plane  $A'_1$  mode ( $172 \text{ cm}^{-1}$ ) and the in-plane  $E'$  mode ( $236 \text{ cm}^{-1}$ ), both present as the characteristic peaks in Raman spectra [21,22,58]. The strong excitation of the two optical phonons originates from the pronounced electron-phonon interaction and can serve as the initial reservoir into which the electronic excitation energy flow (Fig. S5 [25]) [59,60]. Under the harmonic oscillation of the two modes, the shrinking of the Mo–Mo dimer and the wrinkling of Te layers will return to its equilibrium position after one cycle of vibration.

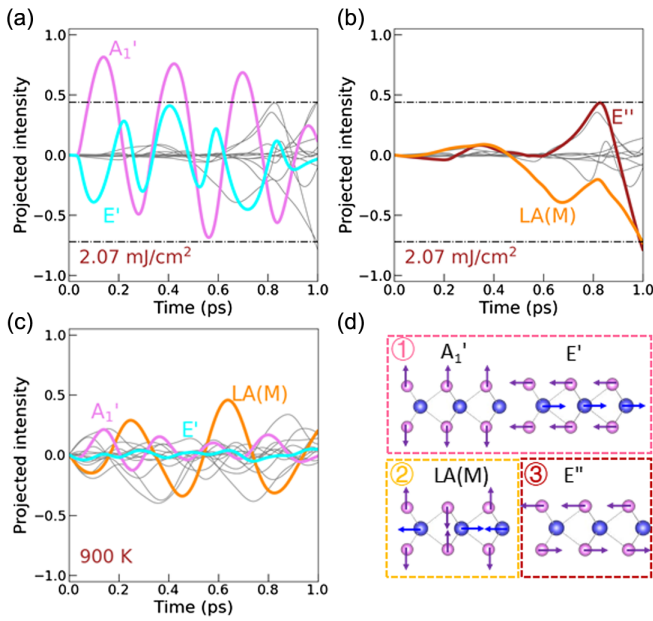


FIG. 3. (a)–(c) Transient atomic displacements projected onto vibrational eigenmodes under the (a)–(b) strong laser field ( $2.07 \text{ mJ/cm}^2$ ) and (c) thermal ( $900 \text{ K}$ ) excitation. (d) Vibrational eigenvectors of four dominant phonon modes.

The observed phase transition is explained through the dephasing, strong damping, and fast mode conversion of the two optical phonon modes. Figure 3(a) shows that at high excitation energy, the amplitude of the initially excited  $A'_1$  and  $E'$  modes are more than 3 times of that in the low-fluence case, leading to the greater distortion that deviates far away from the  $2H$  phase (Fig. S6 [25]). After 0.4 ps, the two modes rapidly transfer their energy to a manifold of modes, among which the  $LA(M)$  and  $E''$  modes are prominent [Fig. 3(b)]. The newly emerged phonon modes successively contribute to the dynamic behaviors described in the last two stages under the strong field excitation [Figs. 2(c)–2(d)]. Compared to the electronic ground state, the decreased vibrational frequencies of the  $A'_1$  and  $E'$  modes indicate the phonon mode softening and the deformation of potential energy surface under the strong laser excitation (Fig. S7 and S8 [25]).

The excitation and coupling of phonon modes are closely related to the relaxation of photoexcited electrons in the conduction bands. It was demonstrated that hot (near band-edge) carriers excited by high (low) energy photons relax by coupling strongly to zone-center optical (zone-edge acoustic) phonons in multilayer MoTe<sub>2</sub> [60]. The single-layer vibrational vectors of the dominant phonons, i.e.,  $A_{1g}$ ,  $E_{2g}^1$  and  $LA(M)$  modes, correspond exactly to the characteristic modes reported in this work. Upon the laser illumination with a photon energy of  $\hbar\omega = 2.34 \text{ eV}$ , the excited electrons occupy high-energy conduction bands and then relax to the band edges via emitting above phonon modes successively in the subpicosecond timescale [Figs. 1(e)–1(f)].

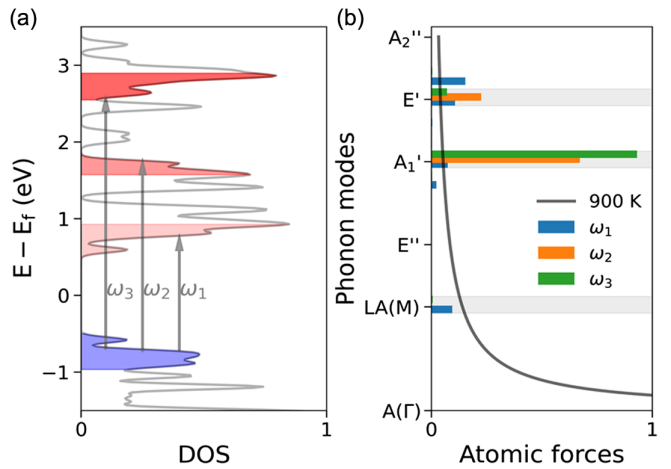


FIG. 4. (a) Schematic of carrier excitation in  $2H$ -MoTe<sub>2</sub> with different laser photon energies of  $\hbar\omega_1 = 1.5 \text{ eV}$ ,  $\hbar\omega_2 = 2.5 \text{ eV}$ , and  $\hbar\omega_3 = 3.5 \text{ eV}$ . (b) Atomic forces projected onto vibrational eigenmodes at the  $\Gamma$  point of the rectangular supercell under photoexcitation and thermal equilibrium.

The forces applied on the ions with fixed electron occupation are shown in Fig. 4. It is clear that when exciting electrons to high-energy conduction bands (i.e.,  $\hbar\omega = 2.5 \text{ eV}$ ), the forces will induce the in-plane and out-of-plane atomic displacements, respectively, along the vibrational eigenvectors of  $E'$  and  $A'_1$  modes, and the  $A'_1$  mode is dominant. The amplitude of excited phonons is linearly dependent on the carrier density (Fig. S9 [25]). However, when electrons are excited to the band edge (i.e.,  $\hbar\omega = 1.5 \text{ eV}$ ), the forces along  $E'$  and  $A'_1$  modes are much decreased, and the atomic movements along the  $LA(M)$  mode emerge. We attribute this intriguing phenomenon to the excitation of the antibonding state within the Mo–Mo dimer (Fig. S10 [25]).

The anharmonic displacement of the optical  $A'_1$  and  $E'$  modes is also essential to trigger phase transitions. Because of the pronounced electron-phonon coupling strength between the  $A'_1(E')$  modes and photoexcited carriers, the driving forces can induce larger transient distortions, e.g., the out-of-plane stretching of the two Te layers is 17.5% of its equilibrium distance at  $t = 0.4 \text{ ps}$ , stores enough energy ( $\sim 0.92 \text{ eV/f.u.}$ ) to overcome the activation energy barrier. Meanwhile, the system is enforced to enter the nonlinear regimes, driving the unidirectional movements along the phase transition pathway (Supplemental Material, Note S9 [25]). The lattice is further deformed along displacement field of other phonons, by reducing their excitation energy (Fig. S11 [25]) [61,62]. Accompanying with the damping of  $A'_1$  and  $E'$  modes and the emergence of  $LA(M)$  mode, the  $2H$  phase has turned to a metallic intermediate state ( $2H^*$ ) where the pattern of Mo–Mo bonds has changed (Note S13 [25]), indicating that 1L-MoTe<sub>2</sub> has transformed from the semiconducting to metallic states within 1 ps.

Carrier cooling that evolves carrier-carrier and carrier-phonon scatterings is a relative fast process for phase transition and induces the consecutive emission of  $A'_1$  ( $E'$ ) and  $LA(M)$  modes, which is in the timescale of  $\sim 0.5$  ps (Fig. S14 [25]). It is expected that on longer timescales, 1L-MoTe<sub>2</sub> will reach a thermal equilibrium and finally transform into a perfect 1T' phase. During this complex process, more phonons in  $q$  space, which are difficult to be discerned, will contribute to the structural distortion simultaneously. For example, after 0.7 ps, apart from the  $E''$  mode, other phonons also emerge. The estimated transition pathway from the 2H\* state to 1T' state is shown in Fig. S15 [25], where the intermediate configurations are generated by linear interpolation. The new transition state has a similar structure to that of the ground-state reaction path [Fig. 1(d)]. Comparing to the ground-state 2H phase, the activation energy barrier between the excited 2H\* to 1T' states has been significantly reduced to  $\sim 0.18$  eV. It indicates a greater transition probability upon photoexcitation, which provides a good explanation for the decreased transition temperature (400 °C) observed in the laser-assisted 1L-MoTe<sub>2</sub> 2H to 1T' phase transition [22].

Photoexcitation allows the ultrafast manipulation of lattice structure within femto- or picosecond, and the phase transition happens before the excited electrons being fully relaxed with their excess energy converted into thermal phonons ( $\sim 10$  ps), during which the carrier distribution, electron-phonon, and phonon-phonon couplings are of vital importance. The selective excitation and the successive scattering of phonon modes are distinct from phase transition driven by thermal phonons. Figure 3(c) shows that upon the thermal activation (900 K), all phonon modes especially the low-energy branches are excited, leading to a rather random phase transition pathway. The relative contribution of  $A'_1$  and  $E'$  modes are decreased and the  $LA(M)$  mode plays the dominant role, obeying the Bose-Einstein distribution in equilibrium [Fig. 4(b)]. As a result, the dynamic behaviors after 0.75 ps are similar to the third stage of photoexcitation [Figs. 2(e)–2(f)]. In contrast to photoexcitation, the shape of potential energy landscape will keep unchanged due to the mutual couplings between different degrees of freedom are not modified [63,64].

Based on above analysis, we make suggestions for selecting laser parameters to enable precise control of nonequilibrium phase engineering: (i) the photon energy should be carefully tuned in the range of  $2.3$  eV  $< \hbar\omega < 3.5$  eV, to excite carriers to unoccupied states that satisfying the strongest electron-phonon coupling; (ii) an intense laser pulse (i.e.,  $J = 2.07$  mJ/cm<sup>2</sup>,  $E_0 = 0.13$  V/Å) with a duration of 20 fs (full width at half maximum) can be applied to excite a high carrier density ( $\eta > 2.42\%$ ) and drive the phonons to the nonlinear regime. In contrast, the weak, long-wavelength laser pulses will only induce the harmonic oscillations around the equilibrium positions of atoms.

The 2H phases are the most common ground state structure in monolayer TMDs, and are the component of various multilayer or bulk materials [65–67]. The similarity and difference of phonon scattering pathways suggest explicit phase engineering strategies for more TMDs (note S16 [25]). The nonequilibrium phonon dynamics can be experimentally detected by time- and momentum-resolved techniques such as the ultrafast electron diffuse scattering (UEDS) [14,68], via monitoring the intensity evolution of Bragg peaks (note S17 [25]). The structural dynamics reported in this work is triggered by photoexcited carriers alone. More discussion about the contribution of Te vacancies is provided in Supplemental Material (notes S18 and S19) [25], which can provide localized states for the concurrent emitting of optical and acoustic phonons, and hence accelerate the phase conversion. In the present work, both electronic and lattice dynamics are robust irrespective of the electron correlation effects, which was reported to have remarkable effect in modulating the band topology of  $T_d$  phase of bulk MoTe<sub>2</sub> (note S20 [25]).

In conclusion, we take 1L-MoTe<sub>2</sub> as a paradigmatic example to show that photodoping induced atomic forces triggers the selective excitation of phonon modes, the ionic vibrational vectors and amplitudes are determined by laser photon energy and intensity. Upon strong-field excitation, the system enters the nonlinear regime and both the electron-phonon couplings and phonon-phonon scatterings contribute to lattice distortions, during which the manipulation of carrier distribution is of vital importance for designing dynamical phase transition strategies. The present work not only offers a detailed understanding of the interplay between the multidegrees of freedom and their dynamical behaviors in the time domain, but also provide principles how the ultrafast control of nonthermal pathways can be achieved in realistic materials. The reported results address the requirements for rational manipulation of material and device performances by laser fields and hence might lead to profound implications.

We acknowledge partial financial support from the National Key Research and Development Program of China (No. 2021YFA1400201), National Natural Science Foundation of China (No. 91850120, No. 11774396, and No. 11934003), and “Strategic Priority Research Program (B)” of Chinese Academy of Sciences (Grant No. XDB330301). M. G. acknowledges support from the China Postdoctoral Science Foundation (Grant No. 2021M693369).

\*These authors contributed equally to this work.

<sup>†</sup>smeng@iphy.ac.cn

- [1] F. Giustino, Electron-phonon interactions from first principles, *Rev. Mod. Phys.* **89**, 015003 (2017).
- [2] A. de la Torre, D. M. Kennes, M. Claassen, S. Gerber, J. W. McIver, and M. A. Sentef, Colloquium: Nonthermal path-

- ways to ultrafast control in quantum materials, *Rev. Mod. Phys.* **93**, 041002 (2021).
- [3] P. Hein, S. Jauernik, H. Erk, L. Yang, Y. Qi, Y. Sun, C. Felser, and M. Bauer, Mode-resolved reciprocal space mapping of electron-phonon interaction in the Weyl semimetal candidate Td-WTe<sub>2</sub>, *Nat. Commun.* **11**, 2613 (2020).
- [4] T. Frigge *et al.*, Optically excited structural transition in atomic wires on surfaces at the quantum limit, *Nature (London)* **544**, 207 (2017).
- [5] A. Lanzara *et al.*, Evidence for ubiquitous strong electron-phonon coupling in high-temperature superconductors, *Nature (London)* **412**, 510 (2001).
- [6] M. Rini, R. Tobey, N. Dean, J. Itatani, Y. Tomioka, Y. Tokura, R. W. Schoenlein, and A. Cavalleri, Control of the electronic phase of a manganite by mode-selective vibrational excitation, *Nature (London)* **449**, 72 (2007).
- [7] R. Merlin, Generating coherent THz phonons with light pulses, *Solid State Commun.* **102**, 207 (1997).
- [8] K. Miyano, T. Tanaka, Y. Tomioka, and Y. Tokura, Photo-induced Insulator-to-Metal Transition in a Perovskite Manganite, *Phys. Rev. Lett.* **78**, 4257 (1997).
- [9] C. Lian, S. J. Zhang, S. Q. Hu, M. X. Guan, and S. Meng, Ultrafast charge ordering by self-amplified exciton-phonon dynamics in TiSe<sub>2</sub>, *Nat. Commun.* **11**, 43 (2020).
- [10] A. Sood *et al.*, Universal phase dynamics in VO<sub>2</sub> switches revealed by ultrafast operando diffraction, *Science* **373**, 352 (2021).
- [11] J. G. Horstmann, H. Bockmann, B. Wit, F. Kurtz, G. Stoeck, and C. Ropers, Coherent control of a surface structural phase transition, *Nature (London)* **583**, 232 (2020).
- [12] A. Zong *et al.*, Dynamical Slowing-Down in an Ultrafast Photoinduced Phase Transition, *Phys. Rev. Lett.* **123**, 097601 (2019).
- [13] M. Na *et al.*, Direct determination of mode-projected electron-phonon coupling in the time domain, *Science* **366**, 1231 (2019).
- [14] M. J. Stern, L. P. René de Cotret, M. R. Otto, R. P. Chatelain, J.-P. Boisvert, M. Sutton, and B. J. Siwick, Mapping momentum-dependent electron-phonon coupling and non-equilibrium phonon dynamics with ultrafast electron diffuse scattering, *Phys. Rev. B* **97**, 165416 (2018).
- [15] M. Mitrano *et al.*, Possible light-induced superconductivity in K<sub>3</sub>C<sub>60</sub> at high temperature, *Nature (London)* **530**, 461 (2016).
- [16] L. Waldecker, R. Bertoni, H. Hubener, T. Brumme, T. Vasileiadis, D. Zahn, A. Rubio, and R. Ernstorfer, Momentum-Resolved View of Electron-Phonon Coupling in Multi-layer WSe<sub>2</sub>, *Phys. Rev. Lett.* **119**, 036803 (2017).
- [17] Q. Wang, E. T. F. Rogers, B. Gholipour, C.-M. Wang, G. Yuan, J. Teng, and N. I. Zheludev, Optically reconfigurable metasurfaces and photonic devices based on phase change materials, *Nat. Photonics* **10**, 60 (2016).
- [18] M. Wuttig and N. Yamada, Phase-change materials for rewriteable data storage, *Nat. Mater.* **6**, 824 (2007).
- [19] D. H. Keum *et al.*, Bandgap opening in few-layered monoclinic MoTe<sub>2</sub>, *Nat. Phys.* **11**, 482 (2015).
- [20] S. Song, D. H. Keum, S. Cho, D. Perello, Y. Kim, and Y. H. Lee, Room temperature semiconductor-metal transition of MoTe<sub>2</sub> thin films engineered by strain, *Nano Lett.* **16**, 188 (2016).
- [21] Y. Wang *et al.*, Structural phase transition in monolayer MoTe<sub>2</sub> driven by electrostatic doping, *Nature (London)* **550**, 487 (2017).
- [22] S. Cho *et al.*, Phase patterning for ohmic homojunction contact in MoTe<sub>2</sub>, *Science* **349**, 625 (2015).
- [23] Y. Li, K. A. Duerloo, K. Wauson, and E. J. Reed, Structural semiconductor-to-semimetal phase transition in two-dimensional materials induced by electrostatic gating, *Nat. Commun.* **7**, 10671 (2016).
- [24] G. Gao, Y. Jiao, F. Ma, Y. Jiao, E. Waclawik, and A. Du, Charge mediated semiconducting-to-metallic phase transition in molybdenum disulfide monolayer and hydrogen evolution reaction in new 1T' phase, *J. Phys. Chem. C* **119**, 13124 (2015).
- [25] See Supplemental Material at <http://link.aps.org/supplemental/10.1103/PhysRevLett.128.015702> for methods and further analysis of the reported data, which includes Refs. [26–50].
- [26] J. C. Tully, Perspective: Nonadiabatic dynamics theory, *J. Chem. Phys.* **137**, 22A301 (2012).
- [27] M. P. Bircher *et al.*, Nonadiabatic effects in electronic and nuclear dynamics, *Struct. Dyn.* **4**, 061510 (2017).
- [28] J. Tully, Mixed quantum-classical dynamics, *Faraday Discuss.* **110**, 407 (1998).
- [29] E. Runge and E. K. U. Gross, Density-Functional Theory for Time-Dependent Systems, *Phys. Rev. Lett.* **52**, 997 (1984).
- [30] C. Lian, M. Guan, S. Hu, J. Zhang, and S. Meng, Photo-excitation in solids: First-principles quantum simulations by real-time TDDFT, *Adv. Theory. Simul.* **1**, 1800055 (2018).
- [31] P. You, D. Chen, C. Lian, C. Zhang, and S. Meng, First-principles dynamics of photoexcited molecules and materials towards a quantum description, *WIREs Comput. Mol. Sci.* **11**, e1492 (2021).
- [32] J. P. Perdew, K. Burke, and M. Ernzerhof, Generalized Gradient Approximation Made Simple, *Phys. Rev. Lett.* **77**, 3865 (1996).
- [33] G. Henkelman, B. P. Uberuaga, and H. Jónsson, A climbing image nudged elastic band method for finding saddle points and minimum energy paths, *J. Chem. Phys.* **113**, 9901 (2000).
- [34] R. Dronskowski and P. E. Bloechl, Crystal orbital Hamilton populations (COHP): energy-resolved visualization of chemical bonding in solids based on density-functional calculations, *J. Phys. Chem.* **97**, 8617 (1993).
- [35] A. R. Attar *et al.*, Simultaneous observation of carrier-specific redistribution and coherent lattice dynamics in 2H-MoTe<sub>2</sub> with femtosecond core-level spectroscopy, *ACS Nano* **14**, 15829 (2020).
- [36] M. A. Py and R. R. J. C. J. o. P. Haering, Structural destabilization induced by lithium intercalation in MoS<sub>2</sub>, and related compounds, *Can. J. Phys.* **61**, 76 (1983).
- [37] Y. Kang *et al.*, Plasmonic Hot Electron Induced Structural Phase Transition in a MoS<sub>2</sub> Monolayer, *Adv. Mater.* **26**, 6467 (2014).
- [38] Y. C. Lin, D. O. Dumcenco, Y. S. Huang, and K. Suenaga, Atomic mechanism of the semiconducting-to-metallic phase transition in single-layered MoS<sub>2</sub>, *Nat. Nanotechnol.* **9**, 391 (2014).
- [39] B. Shang *et al.*, Lattice -mismatch-induced ultrastable 1T-phase MoS<sub>2</sub> – Pd/Au for plasmon-enhanced hydrogen evolution, *Nano Lett.* **19**, 2758 (2019).

- [40] U. Maitra, U. Gupta, M. De, R. Datta, A. Govindaraj, and C. N. R. Rao, Highly Effective Visible-Light-Induced H<sub>2</sub> Generation by Single-Layer 1T-MoS<sub>2</sub> and a Nanocomposite of Few-Layer 2H-MoS<sub>2</sub> with Heavily Nitrogenated Graphene, *Angew. Chem., Int. Ed.* **52**, 13057 (2013).
- [41] Y. Fang *et al.*, Structure Re-determination and Superconductivity Observation of Bulk 1T MoS<sub>2</sub>, *Angew. Chem., Int. Ed.* **57**, 1232 (2018).
- [42] M. Acerce, D. Voiry, and M. Chhowalla, Metallic 1T phase MoS<sub>2</sub> nanosheets as supercapacitor electrode materials, *Nat. Nanotechnol.* **10**, 313 (2015).
- [43] P. Cheng, K. Sun, and Y. H. Hu, Memristive behavior and ideal memristor of 1T phase MoS<sub>2</sub> nanosheets, *Nano Lett.* **16**, 572 (2016).
- [44] K. A. Duerloo, Y. Li, and E. J. Reed, Structural phase transitions in two-dimensional Mo- and W-dichalcogenide monolayers, *Nat. Commun.* **5**, 4214 (2014).
- [45] W. Hou, A. Azizimanesh, A. Sewaket, T. Peña, C. Watson, M. Liu, H. Askari, and S. M. Wu, Strain-based room-temperature non-volatile MoTe<sub>2</sub> ferroelectric phase change transistor, *Nat. Nanotechnol.* **14**, 668 (2019).
- [46] Z. Chen, H. Nan, Z. Liu, X. Wang, X. Gu, and S. Xiao, Effect of thermal conductivity of substrate on laser-induced phase transition of MoTe<sub>2</sub>, *J. Raman Spectrosc.* **50**, 755 (2019).
- [47] X. Dai, Z. Yang, A. Li, J. Yang, and F. Ouyang, Character of defect states in vacancy-doped MoTe<sub>2</sub> monolayer: Spatial localization, flat bands and hybridization gap, *Superlattices Microstruct.* **130**, 528 (2019).
- [48] D. Y. Hwang, K. H. Choi, and D. H. Suh, A vacancy-driven phase transition in MoX<sub>2</sub> (X: S, Se and Te) nanoscrolls, *Nanoscale* **10**, 7918 (2018).
- [49] N. Xu *et al.*, Evidence of a Coulomb-Interaction-Induced Lifshitz Transition and Robust Hybrid Weyl Semimetal in Td-MoTe<sub>2</sub>, *Phys. Rev. Lett.* **121**, 136401 (2018).
- [50] S. Beaulieu *et al.*, Ultrafast dynamical Lifshitz transition, *Sci. Adv.* **7**, eabd9275 (2021).
- [51] M. Chhowalla, H. S. Shin, G. Eda, L. J. Li, K. P. Loh, and H. Zhang, The chemistry of two-dimensional layered transition metal dichalcogenide nanosheets, *Nat. Chem.* **5**, 263 (2013).
- [52] A. V. Kolobov, P. Fons, and J. Tominaga, Electronic excitation-induced semiconductor-to-metal transition in monolayer MoTe<sub>2</sub>, *Phys. Rev. B* **94**, 094114 (2016).
- [53] A. Krishnamoorthy, L. Bassman, R. K. Kalia, A. Nakano, F. Shimojo, and P. Vashishta, Semiconductor-metal structural phase transformation in MoTe<sub>2</sub> monolayers by electronic excitation, *Nanoscale* **10**, 2742 (2018).
- [54] C. Si, D. Choe, W. Xie, H. Wang, Z. Sun, J. Bang, and S. Zhang, Photoinduced vacancy ordering and phase transition in MoTe<sub>2</sub>, *Nano Lett.* **19**, 3612 (2019).
- [55] D. M. Fritz *et al.*, Ultrafast bond softening in bismuth: Mapping a solid's interatomic potential with x-rays, *Science* **315**, 633 (2007).
- [56] W.-H. Liu, J.-W. Luo, S.-S. Li, and L.-W. Wang, Microscopic force driving the photoinduced ultrafast phase transition: Time-dependent density functional theory simulations of IrTe<sub>2</sub>, *Phys. Rev. B* **102**, 184308 (2020).
- [57] S. Gerber *et al.*, Femtosecond electron-phonon lock-in by photoemission and x-ray free-electron laser, *Science* **357**, 71 (2017).
- [58] M. Yamamoto *et al.*, Strong enhancement of Raman scattering from a bulk-inactive vibrational mode in few-layer MoTe<sub>2</sub>, *ACS Nano* **8**, 3895 (2014).
- [59] J.-J. Zhang, B. Gao, and S. Dong, Strain-enhanced superconductivity of MoX<sub>2</sub> (X = S or Se) bilayers with Na intercalation, *Phys. Rev. B* **93**, 155430 (2016).
- [60] A. Krishnamoorthy *et al.*, Optical control of non-equilibrium phonon dynamics, *Nano Lett.* **19**, 4981 (2019).
- [61] M. Först, C. Manzoni, S. Kaiser, Y. Tomioka, Y. Tokura, R. Merlin, and A. Cavalleri, Nonlinear phononics as an ultrafast route to lattice control, *Nat. Phys.* **7**, 854 (2011).
- [62] A. Subedi, A. Cavalleri, and A. Georges, Theory of nonlinear phononics for coherent light control of solids, *Phys. Rev. B* **89**, 220301(R) (2014).
- [63] P. B. Allen, Theory of Thermal Relaxation of Electrons in Metals, *Phys. Rev. Lett.* **59**, 1460 (1987).
- [64] B. Koopmans, G. Malinowski, F. Dalla Longa, D. Steiauf, M. Fahnle, T. Roth, M. Cinchetti, and M. Aeschlimann, Explaining the paradoxical diversity of ultrafast laser-induced demagnetization, *Nat. Mater.* **9**, 259 (2010).
- [65] H. H. Huang, X. Fan, D. J. Singh, and W. T. Zheng, Recent progress of TMD nanomaterials: Phase transitions and applications, *Nanoscale* **12**, 1247 (2020).
- [66] S. Manzeli, D. Ovchinnikov, D. Pasquier, O. V. Yazyev, and A. Kis, 2D transition metal dichalcogenides, *Nat. Rev. Mater.* **2**, 17033 (2017).
- [67] Y. Xiao, M. Zhou, J. Liu, J. Xu, and L. Fu, Phase engineering of two-dimensional transition metal dichalcogenides, *Sci. China Mater.* **62**, 759 (2019).
- [68] L. P. René de Cotret, J.-H. Pöhls, M. J. Stern, M. R. Otto, M. Sutton, and B. J. Siwick, Time- and momentum-resolved phonon population dynamics with ultrafast electron diffuse scattering, *Phys. Rev. B* **100**, 214115 (2019).